Optical Engineering

OpticalEngineering.SPIEDigitalLibrary.org

Finishing of metal optics by ion beam technologies

Jens Bauer
Frank Frost
Antje Lehmann
Melanie Ulitschka
Yaguo Li
Thomas Arnold

SPIE.

Jens Bauer, Frank Frost, Antje Lehmann, Melanie Ulitschka, Yaguo Li, Thomas Arnold, "Finishing of metal optics by ion beam technologies," *Opt. Eng.* **58**(9), 092612 (2019), doi: 10.1117/1.OE.58.9.092612.

Finishing of metal optics by ion beam technologies

Jens Bauer,[a,*] Frank Frost,[a,*] Antje Lehmann,[a] Melanie Ulitschka,[a] Yaguo Li,[a,b] and Thomas Arnold[a,c]
[a]Leibniz Institute of Surface Engineering (IOM), Leipzig, Germany
[b]Fine Optical Engineering Research Center, Chengdu, China
[c]Technische Universität Dresden, Institute of Manufacturing Science and Engineering, Dresden, Germany

Abstract. Ultraprecise mirror devices show considerable potential with view to applications in the visible and the ultraviolet spectral ranges. Aluminum alloys gather good mechanical and excellent optical properties and thus they emerge as important mirror construction materials. However, ultraprecision machining and polishing of optical aluminum surfaces are challenging, which originates from the high chemical reactivity and the heterogeneous matrix structure. Recently, several ion beam-based techniques have been developed to qualify aluminum mirrors for short-wavelength applications. We give an overview of the state-of-the-art ion beam-processing techniques for figure error correction and planarization, either by direct aluminum machining or with the aid of polymer or inorganic, amorphous surface films. [DOI: 10.1117/1.OE.58.9.092612]

Keywords: ion beam figuring; ion beam planarization; plasma-jet deposition; mirrors; aluminum; nickel phosphorus; polymer films.

Paper 190154SS received Feb. 1, 2019; accepted for publication Apr. 16, 2019; published online May 20, 2019.

1 Introduction

Metal optics has attained increasing interest for satisfying the growing needs of high-performance components for short-wavelength optical systems. Aluminum is a widely used mirror construction material because of its low price, good machinability, and a detailed metallurgical knowledge. Technical aluminum alloy materials, such as AL6061, show an excellent shape stability, which is necessary for robust and durable optical devices.[1,2] Optical aluminum surfaces for use in the infrared spectral range are usually fabricated by single-point diamond turning (SPDT).[3–5] However, for short-wavelength applications in the visible (VIS) or even the ultraviolet (UV) range, the requirements on the optical surface quality increase. Apart from a high figure accuracy to allow for best imaging properties, very low surface roughness and waviness values need to be reached. Otherwise, scattering and diffraction losses decrease the optical device efficiency. For VIS and UV spectral range applications, root mean square (rms) roughness values of 1 nm and <0.3 nm need to be targeted, respectively.[6] However, by SPDT, a typical roughness of 2- to 3-nm rms is achievable.[1,7,8] An additional issue is the periodic turning marks with a pitch of 1 to 10 μm distance and up to a few ten nanometers in height. As a result, undesired diffraction effects appear in UV/VIS range applications.

Topography errors on optical surfaces are usually categorized by the spatial frequency of their occurrence (Fig. 1).[9,10] Low-spatial frequency (LSF) errors are found for surface errors below the cutoff frequency f_f separating the figure and the waviness. On the contrary, high-spatial frequency (HSF) error comprises surface errors larger than the cutoff frequency f_c of waviness and roughness. In particular, microroughness is also included in the HSF region, which is separated from roughness by the cutoff frequency f_s. In between the LSF and the HSF, the mid-spatial frequency (MSF) errors are situated. Standard cutoff frequency values are given in Deutsche Industrie-Norm ISO 10110-8:2012-02 as $f_f = 400\ \mathrm{m}^{-1}$, $f_c = 12.5\ \mathrm{mm}^{-1}$, and $f_s = 400\ \mathrm{mm}^{-1}$. However, those values strongly depend on the specific application and, in particular, the applied wavelength of light. The ISO reference wavelength is 546.07 nm. The shorter the wavelength in application, the higher are the cutoff frequencies. Hence, the cutoff frequencies are illustrated as ranges in Fig. 1.

In optical device finishing, the following surface errors are targeted: (1) LSF errors are surface figure errors, i.e., a reduced perfection in the surface shape. Figure errors cause imaging errors as distortions and can be corrected by ion beam figuring (IBF). (2) Regular or irregular error features in the MSF-to-HSF range are waviness and roughness. Prominent feature types are the turning marks from SPDT, which result from the feed of the diamond tool. Furthermore, chatter marks resulting from mechanical vibrations of the turning machine are apparent. Unfortunately, latter are situated in the MSF error range and cannot be corrected so far. Ion beam planarization (IBP) is a common technique to improve the waviness and roughness. (3) Surface errors, which are smaller than the wavelength of light, are microroughness features. As a result of microroughness, the optical surface exhibits a diffusive shine, the so-called halo.[11] Microroughness can also be faced by IBP. For any surface-finishing technique, it is desired to not only improve the surface in the specific spatial frequency range but also take care that the surface is not diminished in another spatial frequency range.

Ion beam technologies offer particular solutions for figure error correction as well as for surface smoothing to qualify optical surfaces (Fig. 2). However, machining of optical aluminum surface is challenging, and not all of the techniques illustrated in Fig. 2 are currently technically mature enough to meet the requirements for UV/VIS range applications. This paper is intended to give an overview of the state-of-the-art ion beam machining techniques available for aluminum mirror finishing, in particular, IBF [Fig. 2(a)] and the

*Address all correspondence to Jens Bauer, E-mail: jens.bauer@iom-leipzig.de; Frank Frost, E-mail: frank.frost@iom-leipzig.de

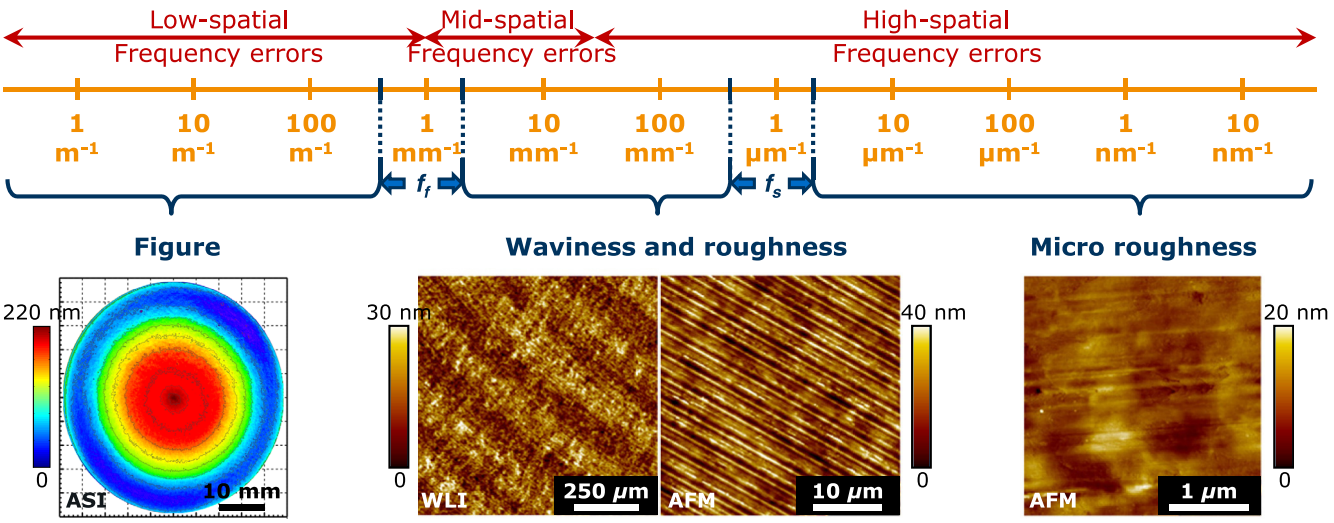

Fig. 1 Error types of optical surfaces to be corrected by ion beam finishing techniques depending on the spatial frequency regimes.

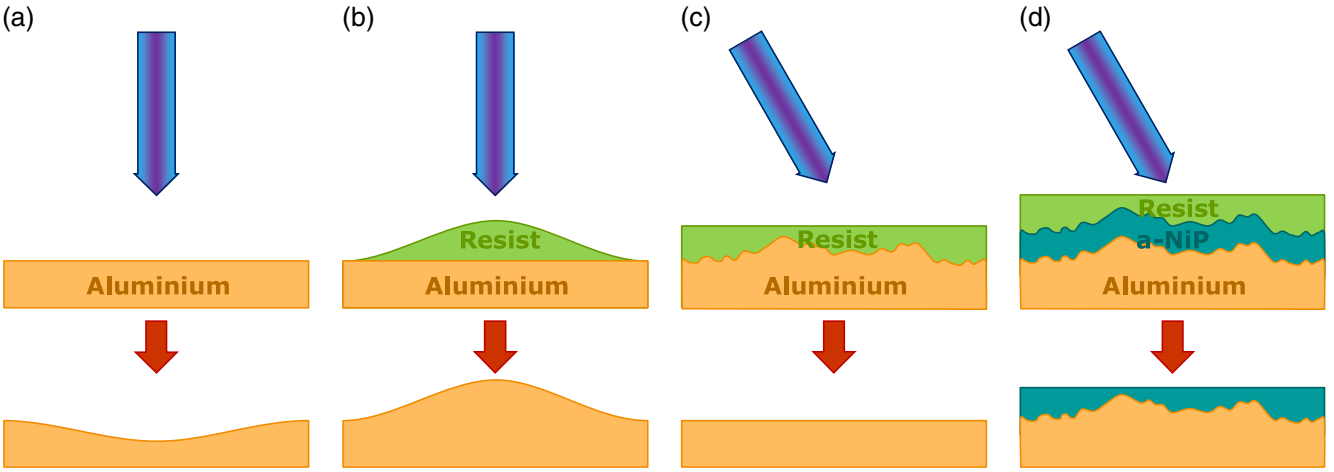

Fig. 2 Schematic overview of the ion beam techniques available to customize optical surfaces: figure error correction by (a) direct IBF and (b) figure mask transfer. IBP for (c) direct surface smoothing and (d) smoothing of an isotropic surface film.

surface smoothing with assistance of an isotropic surface film [Fig. 2(d)]. Resist-related techniques as the figure mask transfer technique [Fig. 2(b)] and IBP [Fig. 2(c)] are presently under development but need to be improved to be applicable to aluminum optics. In Sec. 2, the recent progress in IBF by reactive process control is focused. In Sec. 3.1 polymer deposition techniques as standard spin-coating and innovative plasma-jet deposition strategies are compared. To achieve ultrasmooth optical surfaces, the application of an amorphous nickel-phosphorus (NiP) thin film is an established technique. Recent developments are treated in Sec. 3.2.

2 Figure Error Correction by Deterministic Ion Beam Technology

IBF is a well-established technique for direct figure finishing of optical surfaces.[6,12,13] As a device-finishing technique, IBF is a slow but most accurate and controllable process. Hence, figure error correction is almost aimed at the nanometer scale as the ultimate surface figuring step in the optical device fabrication chain.

The ion beam width is small compared to the optical surface to be machined. Usually low-energy argon or xenon ions ($E < 1.5$ keV) are applied in a pure physical sputter erosion process.[14–19] The reactive ion beam etching (RIBE) technology allows further degrees of freedom since chemical interactions between the ion beam and the substrate material are applied to increase the process' efficiency, e.g., by an increasing etching rate due to the formation of volatile chemical species[20,21] or to improve the surface quality by a chemical modification of the substrate surface during ion irradiation.[22,23]

In principle, the process sequence for figure error correction is as follows: first, a dwell-time algorithm is applied to transfer the figure error profile into a motion map. Afterward, the ion beam is moved deterministically along the device surface following the simulated motion profile. This approach allows the figure error correction of huge and diversely shaped mirror devices. The pathway is s-like in standard operation, but this not a necessity. The pathway can be adapted to the geometry of the special figure-removal profile.

For example, for the figure error correction of a radial symmetric surface error, it can be more advantageous to use sample rotation to reduce the dwell-time problem to a linear motion in radial direction.[24] The smaller the tool size, the higher is the flexibility in the device shape and the higher are the spatial frequency features to be reached during correction. Thus, the deterministic technology approach allows the machining of strongly curved or even free-form optics. With a view to short-wavelength imaging systems, mirror devices often exhibit a complex figured surface with a spherical, aspherical, or free-form shape.[25]

For ion beam generation, a 13.56-MHz transformer-coupled plasma (TCP)-type ion beam source is used.[26] Inert (Ar) or reactive (O_2, N_2) process gas is applied at a beam voltage of $\leq$1.5 kV (Fig. 3). The ion extraction and beam formation is performed by a triple grid system. The grids are spherically concave-shaped. As a result, the ion beam exhibits a constricted region. The working distance is chosen as the point of maximum constriction, i.e., at the smallest beam width. A higher working distance allows better flexibility in sample positioning in front of the ion source during ion-beam processing. The beam constriction and the working distance can be tuned by adjusting the grid curvature.[27] With a curvature radius of 150 mm and a screen grid opening of 10 mm, a narrow ion beam with a full width at half maximum (FWHM) of ~5 mm and a strong ion current density of 8.1 mA/cm^2 are obtained at the working distance of 32 mm [Fig. 3(b)].

The aluminum surface composition is characterized by time-of-flight secondary ion mass spectrometry (TOF-SIMS). For topography analysis, aspherical stitching interferometry (ASI, QED technologies), white-light interferometry (WLI), and atomic force microscopy (AFM) are used. To allow a quantitative topography evaluation, the power spectral density (PSD) function is calculated from the WLI and AFM measurements and rms roughness values are determined within the reliable spatial frequency range, which depends on the particular WLI and AFM measurement conditions (see Ref. 23, for the details on the measurement equipment, PSD evaluation, and roughness calculation).

Usually the figure error correction of optical devices is performed by IBF with Ar gas. However, if this process is applied to aluminum surfaces, a strong degradation is obtained.[28] Defects become enlarged and a huge surface roughening develops. As reasons, a high Al surface mobility and preferential sputtering are addressed.[23]

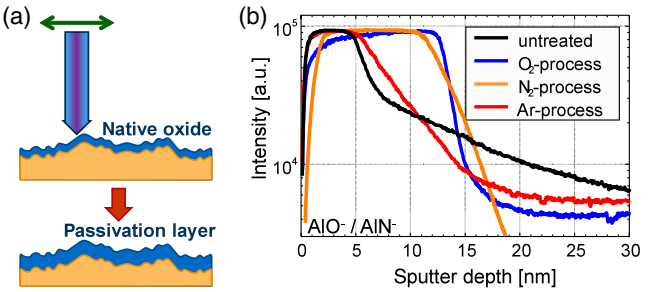

Fig. 4 (a) Sketch: during RIBE treatment a quasistationary near-surface layer is formed as a result of the interplay between ion implantation and sputtering. This surface layer passivates structural and compositional inhomogeneities of the Al matrix. (b) TOF-SIMS depth profiles revealing the formation of the near-surface oxide or nitride layer after RIBE treatment with 1.5-keV oxygen or nitrogen ions, respectively. Note, after ion processing the samples are exposed to the lab environment. Thus, the Ar ion-treated surface exhibits a native oxide layer.

Recently, it has been shown that the application of reactively driven, low-energy ion beam tools allows the direct figure error correction of mirror optics made from aluminum technical alloy materials AL6061 and AL905.[23] Nontoxic gases, such as oxygen and nitrogen, are used for ion-beam processing. As a result of the low-energy reactive ions impacting the aluminum, the surface is chemically modified [Fig. 4(a)]. By the interplay between near-surface ion implantation and sputter erosion, quasistationary surface conditions develop. Hence, a characteristic surface layer is formed with 12- to 15-nm thickness [Fig. 4(b)]. The erosion process rests on the pure physical sputtering, enabling a high degree of process control. Furthermore, the sputtering process occurs within this surface layer exclusively. It is noteworthy that no volatile species is formed during RIBE processing of aluminum surfaces.

The surface layer is very advantageous for the ion beam machining process, because it inhibits the Al-surface mobility efficiently. Furthermore, structural and compositional inhomogeneities of the aluminum are passivated. As a result, the surface roughness is almost preserved during RIBE figuring [Fig. 5(a)]. This conception holds up to 400 nm in depth for the oxygen process[23] and up to 1 μm for the nitrogen process [Fig. 5(b)]. With increasing depths beyond these limits, etch pits emerge, which are related to the heterogeneous Al alloy matrix. In particular, in Al6061, the preferential sputtering of precipitates of Mg_2Si and the

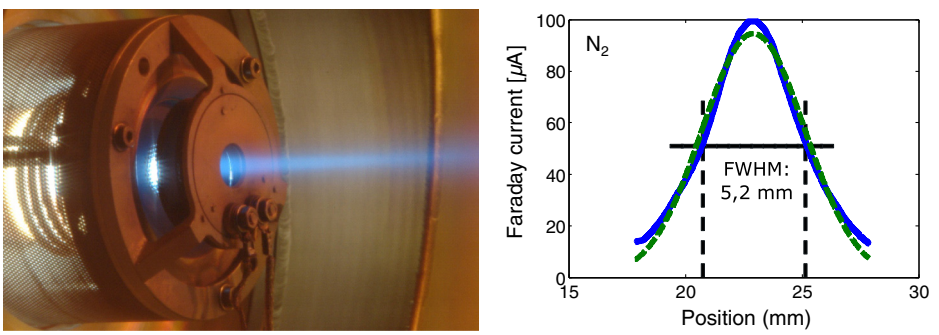

Fig. 3 TCP-type ion source forming a 1.5-keV constricted nitrogen ion beam in operation. *In-situ* Faraday analysis reveals a Gaussian-shaped beam profile with a beam width of about 5 nm.

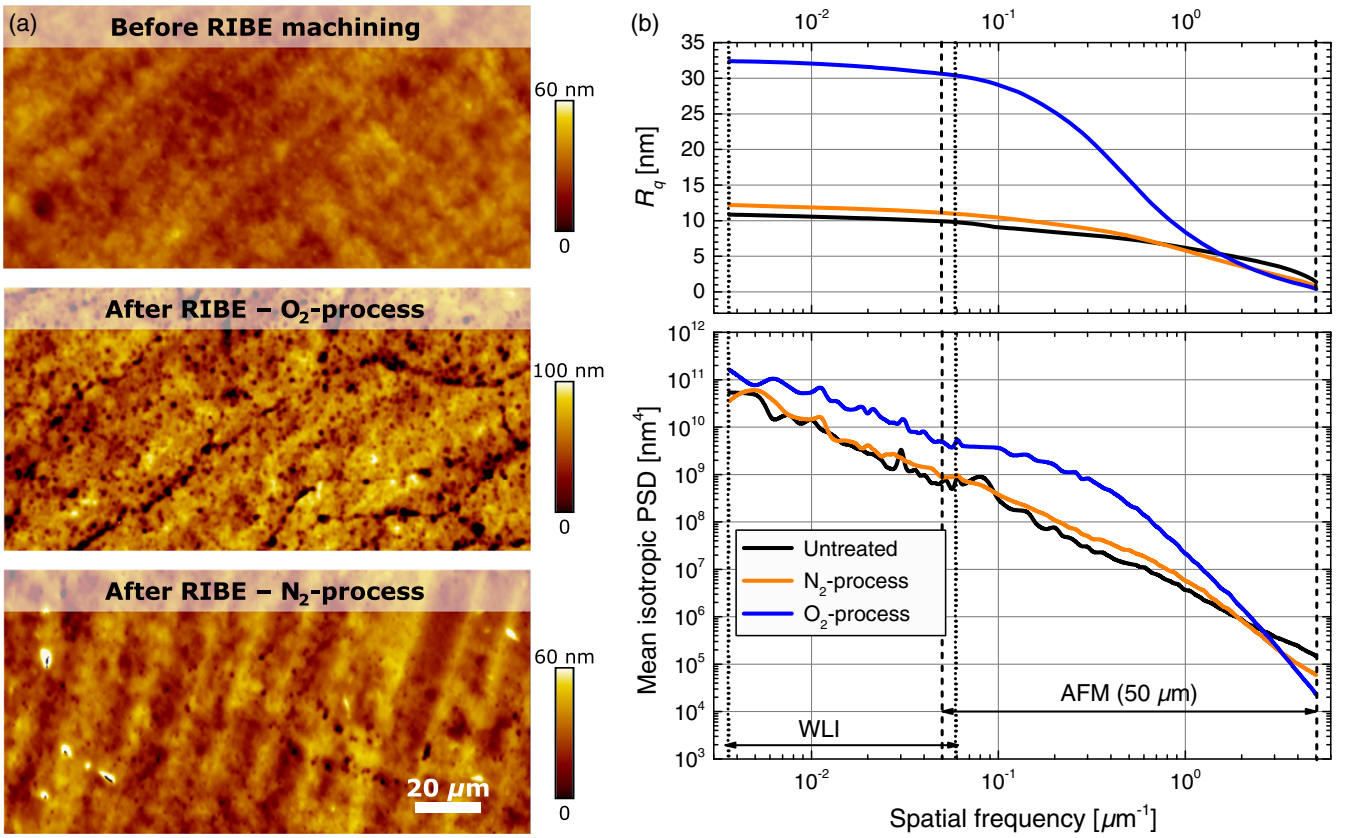

Fig. 5 Al905 surface before and after RIBE machining with the oxygen and the nitrogen processes at 1 μm etching depth. (a) Topographies measured by WLI, (b) PSD, and roughness analysis.

quaternary phase $Al_5Cu_2Mg_8Si_6$ have been identified to cause etch pits.[23] The width of the etch pits ranges within a few micrometers for Al6061, while for Al905 almost submicrometer sized etch pits are apparent. Further investigations are necessary to clarify the etch pit formation in Al905 surfaces. However, for a detailed analysis, it is necessary to know the main alloy constituents. Rapidly solidified aluminum (RSA) from RSP technology is applied. Diverse composition sets are found in literature for the RSA alloy materials. The following composition sets are sorted by descending atomic fraction: Gubbels et al.[29] report on (1) Al6061 containing Mg, Si, and Cu, and (2) Al905 without Si and Mg, but Fe, Cu, Mn, Zr, Mo, and Ni instead. ter Horst et al.[30] found a more complex Al6061 composition with Mg, Si, Fe, Cu, Cr, and little amounts of Ti, Mn, and Zr. Obviously, the compositions of the RSA alloys are not strictly defined and thus need to be analyzed in any development study. Dynamic TOF-SIMS (TOF-SIMS IV, IONTOF) experiments are performed in positive mode on the RSA samples used in this study. For sputtering, a 1-keV oxygen ion beam is used. The analysis is done by a 15-keV Ga ion beam while the analysis scan field of 50×50 μm is centered within the 300×300 μm sputter crater. After 300 s sputtering the surface-related gradients of the mass signals drop out. Beyond the surface region, the following constituents are found qualitatively: (1) Al6061 with Mg, Cr, Mn, Fe, Si, and small amounts of Cu and Ti and (2) Al905 with Ni, Fe, Mg, Mn, Cu, Ti, and Zr as well as traces of Zn, Si, and Cd. Especially the amounts of Mg and Ni in Al905 and Cr, Mn, and Fe in Al6061 are unexpectedly high.

With the RIBE figuring technology, it is now possible to correct the figure error of aluminum mirror surfaces without degradation. Usually surface figuring is an iterative technique, i.e., the figure error is reduced in a stepwise procedure starting from the correction of coarse surface errors with lower spatial frequency. For that reason, aperture-less ion beam tools with a beam width in the range of a few millimeters (as seen in Fig. 3) are applied. The subsequent refinement of the surface figure is achieved by lowering the ion beam width in the next iteration steps. Depending on the figure requirements defined by the application, typically 1 to 4 iteration steps need to be performed. For the present, an ultimate beam width of FWHM $\sim$ 0.6 mm is achievable by applying a contraction aperture,[27] defining the upper spatial frequency limit for figure error correction at $\sim$1.6 mm^{-1} (Fig. 1). Typical removal rates for the nitrogen ion beam process at 1.5 keV on aluminum are 0.80 mm^3/h for an ion beam tool with FWHM $\sim$ 5 mm and 0.003 mm^3/h for FWHM $\sim$ 0.6 mm. The lower the beam width, the lower is the removal rate and thus the higher are the process accuracy and controllability.

Figures 6 and 7 show an example on the coarse figure error correction of a 50-mm diameter planar Al905 disc optics as a first step in the iterative process sequence in RIBE finishing. The figure error after SPDT is radially symmetric, exhibiting a hill of about 220 nm in the center of the sample [Fig. 7(a)]. The task was the reduction of this figure error by 100 nm due to the removal of a best-fit paraboloidal-shaped profile. For this reason, the aperture-less ion beam tool, which is depicted in Fig. 3, is used in deterministic operation via the dwell-time approach. Figure 6(a) shows

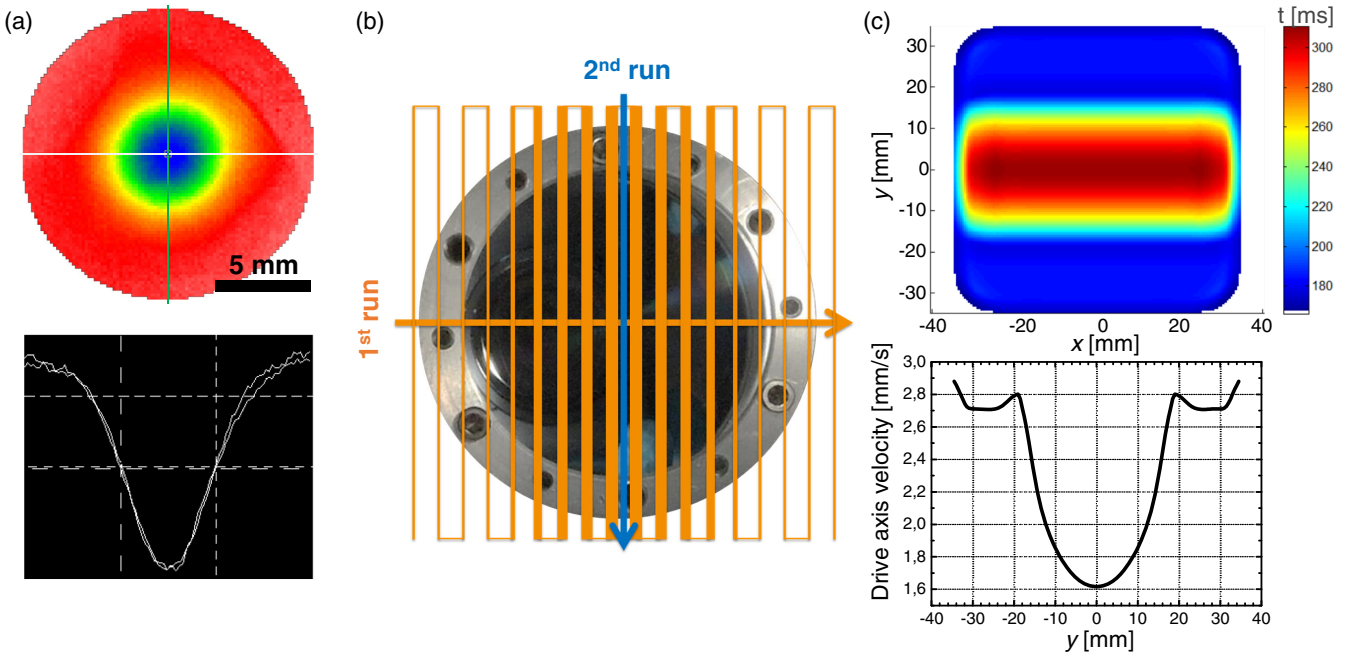

Fig. 6 (a) Footprint profile (FWHM = 5.3 mm) in Al905 by a reactive ion beam (N_2, 1.5 keV, FWHM = 5.2 mm). (b) Sketch of the crossed s-path machining runs. The velocity of the driving axis is varied between the scan lines. A thicker line indicates a slower velocity resulting in a higher local removal. (c) Calculated dwell-time matrix and drive axis velocity profile for the parabolic correction with 50-nm central removal per run.

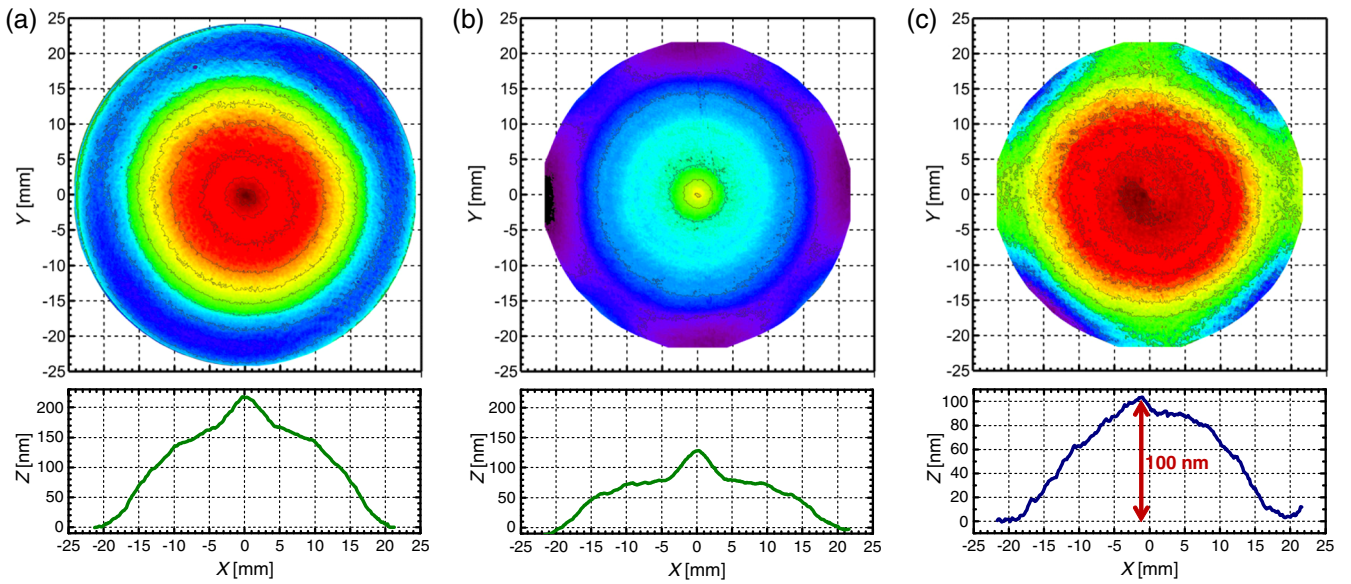

Fig. 7 Paraboloidal correction of a diamond-turned Al905 disc optics by RIBE (N_2, 1.5 keV, FWHM = 5.2 mm). Interferometry images (a) as diamond-turned, (b) after RIBE correction, and (c) removal profile (difference of a and b).

a footprint etching in Al905. The footprint profile reproduces the Gaussian tool function excellently in shape and size. Hence, the reactive ion beam exhibits a proportional material removal, which is an essential requirement for a deterministic machining scheme. A crossed machining procedure with two perpendicular runs has been chosen [Fig. 6(b)]. First, a parabolic correction with a 50-nm center removal is performed. Then a second correction is done by an additional perpendicular run. The deterministic machining is performed by s-like scan paths with an equal line pitch of 0.5 mm to allow a sufficient scan line overlapping. On each scan line the drive axis velocity is held constant, but the velocity is varied from line to line to merge the individual line removal characteristics into a parabolic removal profile. A dwell-time simulation is calculated to determine the drive axis velocity profile resulting in the best-fit parabolic removal [Fig. 6(c)].

Figure 7(b) shows the residual figure error after the ion beam correction by the crossed machining procedure. The corresponding removal profile [Fig. 7(c)] exhibits the intended paraboloidal shape with the 100-nm central removal. At the device borders some deviations owing a fourfold asymmetry appear, which are caused by the quadratic scan field geometry.

3 Surface Smoothing by Low Energy Ion Beam Techniques

3.1 *Polymer Resist-Related Ion Beam Techniques*

The deposition of polymer film masks for use in the mask transfer technique has been investigated by atmospheric plasma-jet deposition with methane as a film-forming agent.[31] The plasma-jet system employed for thin film deposition has been originally developed for atmospheric pressure plasma etching, where very high spatiotemporal stability of the plasma discharge is required.[32–34] High frequency power is used to ignite and sustain the plasma. The plasma-jet source consists of a coaxial conductor system [Fig. 8(a)]. The inner conducting electrode forms at the same time as the feeding gas tube. The body of the plasma source acts as outer conductor of the coaxial system. The system is tuned in a manner that maximum electric field strength is ensured at the outlet of the inner tube electrode. There, the jet-like plasma of ∼10-mm length is discharged. The source is mounted on a three-axis computerized numerical control stage to enable a relative motion over the substrate surface. The plasma jet is fed by 900 sccm helium as carrier gas. The layer-forming precursor is methane with a flow rate of 5 sccm. A peripheral nitrogen-shielding gas flow of 350 sccm prevents the entrainment of surrounding air into the plasma and ensures spatial stability of the jet. Plasma excitation is performed by microwave at 2.45 GHz, applying short pulses of 5 μs at a repetition rate of 6 kHz and peak power of 200 W. On an average, a power of 6 W is dissipated, which maintains a surface temperature slightly above the room temperature. Under static conditions, where the plasma source is not moved, thin film deposition occurs on substrates in the form of a Gaussian footprint exhibiting a FWHM of ∼1 mm and a maximum deposition rate of 160 nm/s. Homogeneous film deposition is performed by raster path motion on a 20×20 mm^2 area on silicon substrate. Total thickness of the films is determined by reflectometry to be ∼190 nm. The film composition strongly depends on the process gas composition and the plasma-jet parameters.[35–37] The x-ray photoelectron spectroscopy (XPS) analysis at the deposited polymer films has revealed a composition relation of $C:N:O \approx 4:2:1$ from C 1s peak asymmetry evaluation [Fig. 8(b)]. Furthermore, strong hydrogen group bands as NH and CH_x are observed in the Fourier-transform infrared spectroscopy (FTIR) fingerprint [reference plot in Fig. 9(a)].

The polymer films are machined by RIBE applying the nitrogen process. The aperture-less configuration (Fig. 3) is used with a beam width of FWHM ∼10 mm at 600 eV and FWHM ∼17 mm at 1200 eV ion energy. The polymer film samples are covered by a graphite hard mask with a circular 13 mm opening to obtain a distinct machining field edge. A homogeneous etching is performed by s-like scanning of a 21-mm-sized scan field over the mask opening with 3 mm/s scan velocity and 3 mm scan line pitch. The machining duration is 65 s. The effect of RIBE on the polymer structure is analyzed by FTIR. In particular, the choice of the ion energy considerably influences the polymer matrix [Fig. 9(a)]. After RIBE at 600 eV, the general FTIR footprint is maintained corresponding to the initial polymer film before RIBE (reference plot). In contrast, after RIBE at 1200 eV, the dominating FTIR peaks in the range of 1700 to 2700 cm^{-1} are strongly diminished. The corresponding vibrational bands refer to multiple bound fractions within the polymer matrix. This result indicates either a higher degree of crosslinking or matrix fragmentation by release of less-bound groups or chain cracking and thus polymer degradation caused by the ion irradiation. In Fig. 9(b), the etching rate during RIBE machining is focused. For the usual case of sputter erosion as a pure physical process, it is expected that the higher the ion energy, the higher the etching rate would be. This situation holds for photoresist and aluminum. However, the polymer films exhibit an opposite behavior. In accordance to the FTIR results, it is suggested that the crosslinking of the polymer, which is intensified by a higher ion energy, results in a higher resistivity in RIBE processing.

To achieve a higher RIBE resistivity, diverse postdeposition treatment procedures have been tested: (1) exposure to 365 nm UV light for 45 min (UVA), (2) exposure to 172 nm UV light for 5 min (UVC), and (3) thermal treatment for

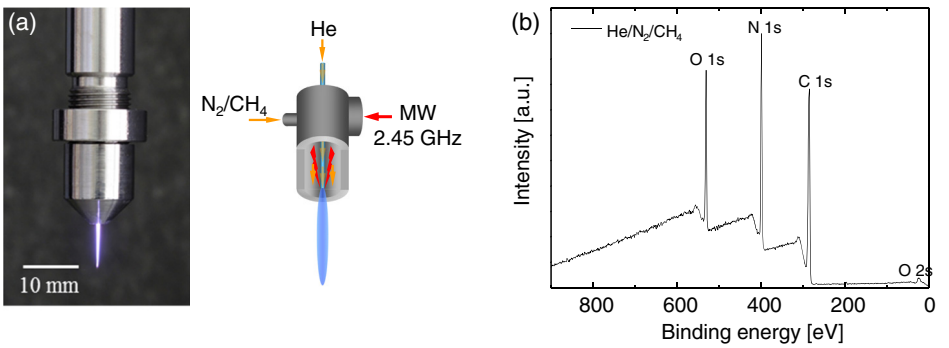

Fig. 8 (a) Microwave-driven plasma-jet tool used for local polymer deposition. Helium is supplied through the inner capillary,while a cold plasma is generated by 2.45-GHz microwave heating. Methane acting as the polymer-forming agent is admixed to the nitrogen shield gas, which homogeneously surrounds the helium plasma torch. (b) XPS analysis of the polymer film revealing a composition relation of $C:N:O \approx 4:2:1$.

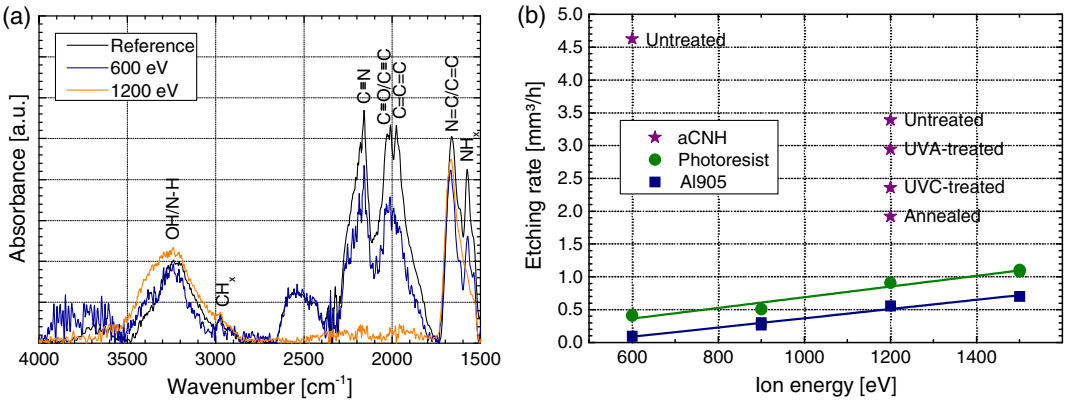

Fig. 9 (a) FTIR measurement of untreated polymer films before and after RIBE machining. Multiple bonds within the polymer matrix are destroyed by ion beam treatment at 1200 eV. (b) Etching rate during RIBE machining with respect to the ion energy. The etching rate shows a general trend for the investigated materials: polymer films > photoresist > aluminum.

10 min at 100°C and 10 min at 200°C. For all treatment procedures, an increased RIBE resistivity, i.e., a reduction of the etching rate, is obtained [Fig. 9(b)]. However, the treatments cause a shrinkage of the deposited film thickness (Table 1). An ideal postdeposition treatment would result in marginal polymer shrinkage, but strong decrease of the polymer etch rate in the RIBE process. As seen in Table 1, shrinkage and rate decrease develop with similar tendencies for the UVC treated and the annealed case. Hence, both effects level out each other to a considerable degree. The overall etching time necessary to remove the complete polymer film on the machined area A can be calculated from the deposited film thickness d_0, shrinkage s, and the etching rate R after postdeposition treatment:

$$t = \frac{A \cdot d_0 \cdot (1+s)}{R} = \frac{A \cdot d_0}{R_{\text{ref}}} \cdot \frac{1+s}{1+r}. \tag{1}$$

The relative etching rate decrease r refers to the etching rate R_{ref} of the untreated polymer film. As a measure, an effective process efficiency yield f can be defined as

$$f = \frac{1+s}{1+r} - 1. \tag{2}$$

The f-values are summarized in Table 1 for the different treatment procedures. As a result, there is a ~20% effective increase in process efficiency for UVC irradiation and annealing, compared to the untreated polymer case, meaning that the overall etching time is prolonged for both kinds of treatment to a very similar extent. Hence, the resistance of the polymer film is effectively increased, thereby lowering the etch selectivity. In contrast, for the UVA treatment, a negative efficiency yield is found. Thus, the UVA treatment is disadvantageous for process improvement. The effective selectivity values in Table 1 include the effect of shrinkage due to post-treatment:

$$S_{\text{eff}} = \frac{R_{Al}}{R} \cdot (1+s) = \frac{R_{Al}}{R_{\text{ref}}} \cdot (1+f) = S_{\text{ref}} \cdot (1+f). \tag{3}$$

The selectivities reported are far beyond unity. Thus, the present plasma-jet-deposited layers are not appropriate for IBP processing. However, these films are interesting to use in the figure transfer technique. The figure error topography has to be converted into a modulated polymer thickness map profile. This map profile is given by the figure error profile, which has to be multiplied by the reciprocal of the effective selectivity value, which is given as the stretching factor m in Table 1. Hence, the thickness profile has to be stretched by a factor of 5 to 7, compared to the actual figure error profile. In principle, the height accuracy should be improved due to the stretching. However, one issue in film topography deposition is the realization sufficient steep slopes to correctly reproduce the error topography. But a stretching of the profile involves a stretching of the slopes particularly. The steeper the slopes, the smaller the

Table 1 Evaluation of an effective process efficiency yield and an effective process selectivity value with respect to the applied postdeposition treatment procedure. The deposited film thickness prior to the treatments is ~190 nm. The effective process efficiency yield is reduced by the thickness shrinkage during the postdeposition treatment and is increased by the etch rate decrease in RIBE machining. UVC and annealing are roughly equally advantageous.

Polymer treatment	Thickness (shrinkage s)	RIBE depth (rate decrease r)	Effective process efficiency yield f	Eff. selectivity (stretching m)
As deposited	189 nm (±0%)	105 nm (±0%)	±0%	0.164 (6.1)
UVA	152 nm (−20%)	91 nm (−13%)	−7%	0.152 (6.6)
UVC	158 nm (−16%)	73 nm (−30%)	+20%	0.197 (5.1)
Annealed	126 nm (−33%)	59 nm (−13%)	+19%	0.194 (5.1)

Table 2 Effect of the postdeposition procedures on the rms roughness (R_q) of the polymer film before and after RIBE machining. The roughness values are determined by WLI in the spatial frequency range of $(3.6 - 60) \cdot 10^{-3}$ μm^{-1}.

Polymer treatment	R_q before RIBE	R_q after RIBE
As deposited	(0.52 ± 0.08) nm	(0.63 ± 0.07) nm
UVA	(0.43 ± 0.04) nm	(0.49 ± 0.05) nm
UVC	(0.47 ± 0.04) nm	(0.52 ± 0.05) nm
Annealed	(0.49 ± 0.07) nm	(0.51 ± 0.04) nm

plasma-jet tool width to be chosen should be. The dependence of the tool width on the deposition rate follows a squarish relation. As a result, the profile stretching prolongates the deposition time by two factors: (1) corresponding to the stretching, a higher film thickness is needed to completely capture the error heights by the RIBE process and (2) the plasma-jet tool size has to be reduced to meet the requirements on the increased slope values, which are necessary to achieve an accurate reproduction of the stretched figure error profile.

An important property of either resist-related ion beam technique is the surface roughness. In Table 2, the surface roughness is summarized for the different postdeposition procedures. In general, the polymer films are very smooth with $R_q \sim 0.5$ nm after deposition. The UVA treatment even slightly improves the roughness. After UVC irradiation and annealing, the initial roughness is preserved. During RIBE machining, the untreated polymer film increases in roughness to minor extent. All postdeposition-treated films exhibit the initial roughness of ~0.5 nm also after RIBE instead. Hence, postdeposition treatment is advantageous to maintain the surface roughness during RIBE machining. In general, from the geometrical point of view, a higher profile stretching should result in a reduction of the surface roughness. However, comparing the stretching factors in Table 1 and the roughness values after RIBE in Table 2, such a trend cannot be observed in the present study. In contrast, the roughness values for all post-treated procedures are almost equal. Note, in addition to the geometrical influence resulting from the thickness stretching, structural effects within the polymer matrix can also contribute to the ultimate roughness after RIBE. Further experiments are necessary to account for structural changes in relation to diverse post-treatment processing procedures and the subsequent behavior under ion irradiation. Those should include: (a) the state of cross linking, (b) polymer matrix degradation effects, (c) the release of less-bound groups by energy impact, (d) reactive ion implantation and incorporation into the matrix, and (e) stoichiometry changes as a result of the component-wise different sputtering yields.

As mentioned earlier, so far the plasma-jet-deposited layers are no option for use in direct IBP. Spin-coated photoresist layers [see Fig. 9(b)] exhibit a higher selectivity of ~0.6 related to aluminum in the ion energy range of 0.9 to 1.5 keV. However, these selectivity values are also even far from unity. Improved planarization layer materials need to be found to establish an efficient, direct IBP approach.

3.2 *Ultrasmooth Optical Surfaces with Aid of an Isotropic Surface Layer*

At present, the direct smoothing of optical aluminum surfaces by IBP, magnetorheological finishing (MRF), or chemical mechanical polishing (CMP) is not sufficient to reach a surface roughness of ≤1.0 nm rms,[38–40] which is a necessity for its application in the UV/VIS spectral range. For this reason, an alternative technological solution has been established. The aluminum device is coated with an amorphous film to allow an improved surface smoothing. Rather than the heterogeneous matrix of an aluminum alloy, a structurally and chemically isotropic material allows a much better machinability in SPDT as well as in ion beam machining. Amorphous materials, such as a-Si or NiP, are common materials in optics fabrication.[41–44] The a-Si can be produced by magnetron sputtering or plasma-enhanced chemical vapor deposition.[45] The NiP is deposited in an electroless approach from an electrolytic bath.[46] In contrast to galvanic deposition, no electric current is applied and the nickel is provided from the bath or by a salt. To increase the reflective surface properties of both amorphous materials, usually a further metallization layer (e.g., Au, Ag) is needed. A major drawback of NiP-coated optics is the mismatch in the coefficients of thermal expansion (CTE) between coating and aluminum. Especially under thermal load conditions, severe issues can arise, e.g., bending due to the bimetallic effect and NiP delamination.[47] For the same reason, lightweight device architectures with low material thickness are strongly limited, if NiP coatings are necessary.[38] Alternative aluminum alloy compositions as AlSi40 with improved CTE matching are under consideration.[48]

However, for the present, NiP is the material of choice for fabricating UV/VIS mirror optics, because it is well-shapeable and reveals ultrasmooth surfaces after IBP.[49,50] Main goals for IBP are the reduction of the regularly aligned and distributed turning marks resulting from SPDT as well as the broadband smoothing of the optical surface in the roughness and the microroughness spatial frequency range (see Fig. 1). For the study, typical NiP samples after SPDT with turning marks with spacings of 1.5, 3.5, 6, and 25 μm and heights of 10, 20, and 60 nm are applied. A spray-coating resist (SX AR-PC 5000/22.4, Allresist GmbH, Germany) with thickness ranging between 170 and 300 nm is used as planarization layer. The higher the resist layer thickness, the better is the smoothing behavior.[50]

Ar ion processing is performed by a Kaufman-type broad-beam ion source with 700-V beam voltage. A two-grid extraction system with 180-mm grid opening is applied. The corresponding Ar ion beam has a beam width of 120 to 150 mm (FWHM) and a beam current of 70 mA. Prior to IBP processing, the angle dependencies of the etching rates of photoresist and NiP are analyzed [Fig. 10(a)]. The working point for IBP is defined by the intersection point of both curves to achieve a selectivity near unity. Hence, following a planarization angle of 35 deg with an etching rate of 10 to 12 nm/min is applied for ion-beam processing.

The topography is tracked by AFM analysis during all stages of IBP processing [Fig. 10(b)]. An NiP surface with turning marks having 1.5 μm spacing and 20-nm height shows a rms roughness of ~6.4 nm after SPDT. A considerable surface smoothing toward ~2.0 nm rms is achieved by deposition of the photoresist planarization layer. By

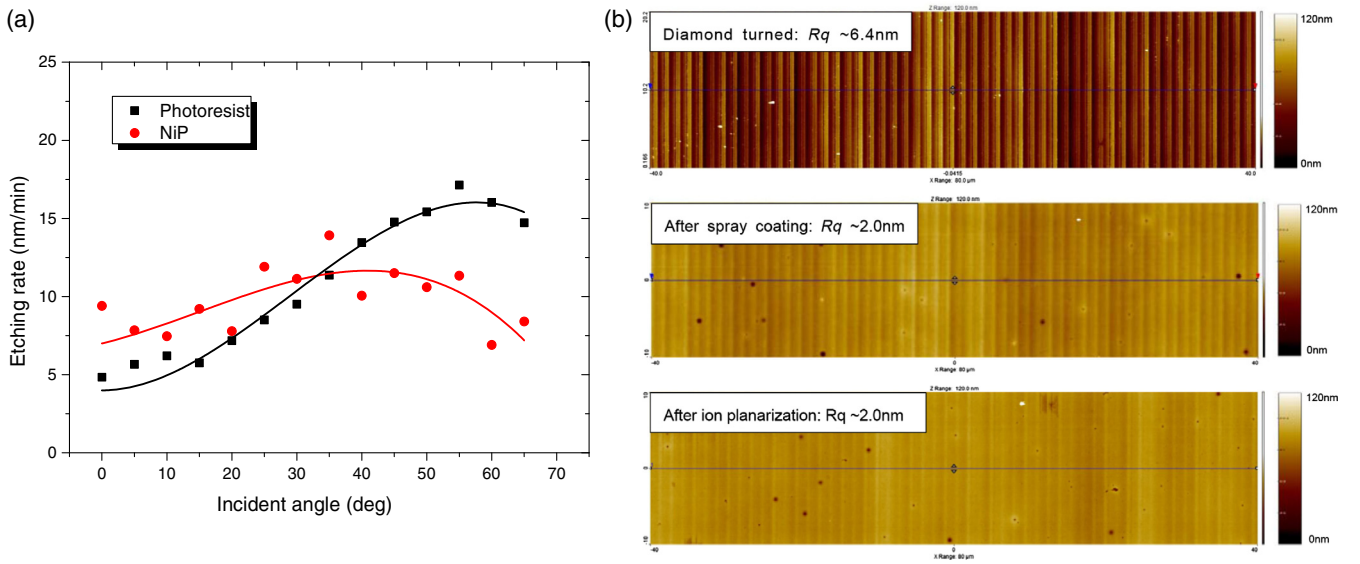

Fig. 10 (a) Effect of the ion beam incidence angle on the etching rate of photoresist and NiP. The crossing at ~30 deg–35 deg, where the etching rate between both materials becomes equal, defines the working point for IBP with a selectivity near unity. (b) AFM images (80 μm × 20 μm) revealing the topography evolution during different stages of the planarization process (turning marks: 1.5 μm spacing/20 nm height). The turning mark features resulting from SPDT are leveled out by the photoresist coverage. During ion-beam processing, the smooth photoresist surface is transferred into the NiP surface. As a remarkable result, the rms roughness is improved starting from ~6.4 to ~2.0 nm after IBP.[49]

means of argon ion beam treatment, this smooth topography is transferred into the NiP surface. As a result, the smooth topography of the planarization layer is fully maintained in the NiP after IBP. Hence, the IBP process exhibits a roughness decrease of about 60% to 70% during a single-process cycle.

In this study, the resist is completely removed after 30-min ion-beam processing. To attain more detailed information about process stability and controllability, the temporal evolution during Ar ion treatment is examined at NiP surfaces with turning marks having 6-μm spacing and 60-nm height [Fig. 11(a)]. Up to 60 min of processing time after complete resist removal, the surface roughness is kept constant at the value of ~6.4 nm rms. A more detailed view on the surface topography reveals no apparent qualitative degradation [Fig. 11(b)].

A much improved surface smoothing can be obtained by iterative IBP processing (Fig. 12). In addition to the significant reduction of the turning mark features, the broadband roughness is considerably decreased after each IBP run cycle [Fig. 12(a)]. As a result, a decrease of ~88% in surface roughness is obtained after four to five IBP run cycles [Fig. 12(b)]. Note, the strongest roughness reduction with ~70% shows already after the first IBP run cycle. During second to forth IBP run cycle, the improvement is already at 20% to 25% per cycle. Beyond four IBP runs, the

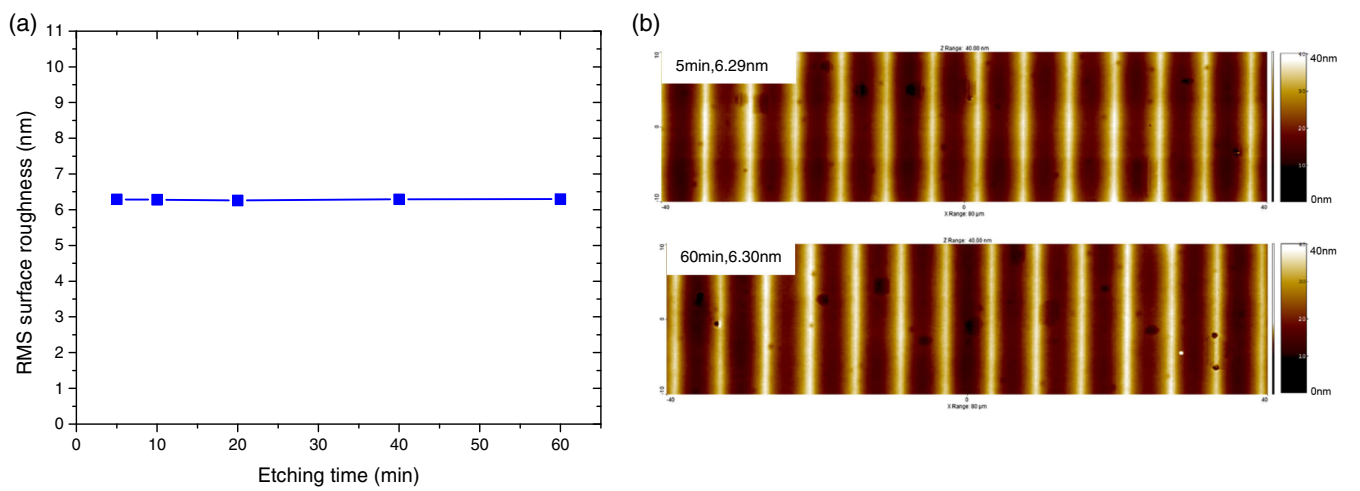

Fig. 11 Effect of the etching time in IBP processing after complete resist removal (turning marks: 6 μm spacing/60 nm height). (a) The rms surface roughness is constant up to 60-min ion beam etching. (b) AFM images (80 μm × 20 μm) at 5 and 60 min etching time showing an unchanged surface topography.[49]

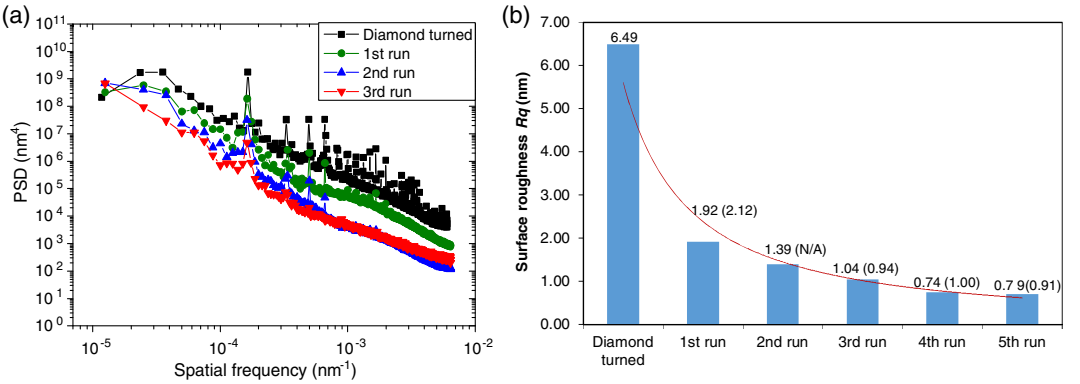

Fig. 12 The topography is improved by iterative IBP processing. (a) Evolution of the PSD function before and after the iterative steps (turning marks: 6 μm spacing/20 nm height). A broadband decrease of the PSD functions is observed with increasing iteration number. Furthermore, the peak features representing the turning marks diminish progressively. (b) The rms roughness decreases exponentially with increasing iteration number (turning marks: 1.5 μm spacing/20 nm height). After a fivefold IBP iteration sequence, the surface roughness decreases from initially ~6.5 to ~0.8 nm after IBP.[50]

surface topography reaches an ultimate smoothness. Further improvement by IBP is not obtained. With a residual roughness of 0.7 to 0.8 nm rms, IBP reveals similar surface qualities as a recently reported NiP smoothing approach, which is based on a combination of MRF and postpolishing.[51] In addition, a very low surface roughness of 0.3 nm rms for NiP has been reported by a combination of fluid jet polishing and bonnet polishing.[52] However, the results are based on WLI measurements, which are limited in the range of microroughness, and thus are not fully comparable to this study. An alternative approach to NiP could be a coating of pure aluminum on the optical surface, which can be smoothed more easily <1.0 nm rather than technical aluminum alloy material by conventional techniques as CMP.[53] Future work has to be done to test this conception also with IBP. However, for complex figured mirror surfaces, a homogeneous aluminum coating could become a challenging issue.

In summary, ion beam technologies exhibit the following diverse capabilities in finishing of aluminum-based optics.

1. Direct figure error correction of optical aluminum surfaces: IBF with a reactive process control is a most promising technique for a direct figure correction approach on optical aluminum surfaces. RIBE allows an improved process control for aluminum surface machining. The use of oxygen or nitrogen process gas permits etching depth up to 400 nm and 1 μm, respectively, while the surface topography is almost preserved in its initial state. Beyond these depth limits, surface degradation by etch pit formation is observed. These etch pits are related to the heterogeneous aluminum alloy matrix. In Al905, smaller etch pits are obtained than in Al6061 material. As a result of the interplay between implantation of the low-energy ions and sputter erosion, the etching process is based on the formation of a quasistationary passivation layer in the 12- to 15-nm near-surface region. Narrow ion beam tools with 0.6 mm up to a few millimeters in width are available to successfully perform figure error correction without surface roughening.
2. Plasma-jet deposition of customized polymer films for use in the figure mask transfer technique: The polymer deposition by the deterministic atmospheric plasma-jet technology allows the surface coating with a customized figure mask. Afterward, this figure mask is transferred into the aluminum surface by RIBE processing. Corresponding to the etching selectivity of <1, the figure mask profile has to be stretched compared to the figure error profile. Since the error profile is converted into a local thickness modulation within the figure mask, the transfer can then be done by use of a broad beam ion source. Further studies are necessary to evaluate this approach in optical device fabrication.
3. IBP of NiP-based optical surfaces: Surface smoothing by IBP is reached by the topography leveling properties of the resist planarization layer. A proper estimation of the geometric conditions during ion-beam processing is necessary to allow a loss-less transfer of the smooth planarization layer topography into the NiP surface. The smoothing effect is improved by usage of increased resist layer thickness and iterative IBP processing. Consequently, the surface roughness can be reduced by up to ~88% after four to five IBP run cycles. The residual surface roughness of 0.7- to 0.8-nm rms after IBP permits high-performance optical applications in the visible spectral range.

Acknowledgments

We are grateful to the IOM workshop and to T. Liebeskind for sample preparation. D. Hirsch is thanked for his assistance in XPS and SIMS measurements. U. Decker and I. Reinhardt are acknowledged for the Fourier-transform infrared spectroscopy analyses. Financial support by the German Federal Ministry of Education and Research (BMBF) within the framework of the InnoProfile Transfer initiative 03IPT706X "Ultra-precision manufacturing using atomic particle beams" is gratefully acknowledged. The authors have nothing to disclose.

References

1. D. Vukobratovich and J. P. Schaefer, "Large stable aluminum optics for aerospace applications," *Proc. SPIE* **8125**, 81250T (2011).

2. T. Newswander et al., "Aluminum alloy AA-6061 and RSA-6061 heat treatment for large mirror applications," *Proc. SPIE* **8837**, 883704 (2013).
3. M. Suganuma et al., "Aluminum-made 5-cm reflecting telescope for Nano-JASMINE," *Proc. SPIE* **6265**, 626545 (2006).
4. I. J. Saunders et al., "Fabrication and metrology of freeform aluminum mirrors for the SCUBA-2 instrument," *Opt. Photonics* **5869**, 586905 (2005).
5. S. Risse et al., "Ultra-precise manufacturing of aspherical and freeform mirrors for high resolution telescopes," *Proc. SPIE* **9151**, 91510M (2014).
6. M. Weiser, "Ion beam figuring for lithography optics," *Nucl. Instruments Methods Phys. Res. Sect. B Beam Interact. Mater. Atoms* **267**(8–9), 1390–1393 (2009).
7. G. P. H. Gubbels, B. W. H. Venrooy, and R. Henselmans, "Accuracy of freeform manufacturing processes," *Opt. Manuf. Test.* **7426**, 742607 (2009).
8. Y.-C. Cheng et al., "Investigation of diamond turning: of rapidly solidified aluminum alloys," *Proc. SPIE* **9192**, 919214 (2014).
9. J. M. Bennett, "Recent developments in surface roughness characterization," *Meas. Sci. Technol.* **3**, 1119–1127 (1992).
10. J. E. Harvey and A. K. Thompson, "Scattering effects from residual optical fabrication errors," *Proc. SPIE* **2576**, 155–174 (1995).
11. H. Bennett and J. Stanford, "Structure-related optical characteristics of thin metallic films in the visible and ultraviolet," *J. Res. Natl. Bur. Stand. Sect. A Phys. Chem.* **80A**, 643 (1976).
12. M. Zeuner and S. Kiontke, "Ion beam figuring technology in optics manufacturing," *Opt. Photonik* **7**, 56–58 (2012).
13. L. Zhou et al., "One-dimensional ion-beam figuring for grazing-incidence reflective optics," *J. Synchrotron Radiat.* **23**, 182–186 (2016).
14. N. Taniguchi and N. Kanekama, "On the ion beam sputter-machining of aspherical surface lens," *Bull. Japan Soc. Precis. Eng.* **7**(1), 29–30 (1973).
15. F. Bigl, T. Hänsel, and A. Schindler, "Oberflächenpräzisionsbearbeitung mit Ionenstrahlen," *Vak. Forsch. und Prax.* **10**(1), 50–56 (1998).
16. T. Hänsel et al., "Ultra-precision surface finishing by ion beam techniques," *Vak. Forsch. und Prax.* **19**(5), 24–30 (2007).
17. P. Gailly et al., "Roughness evolution of some X-UV reflective materials induced by low energy (<1 keV) ion beam milling," *Nucl. Instruments Methods Phys. Res. Sect. B Beam Interact. Mater. Atoms* **216**, 206–212 (2004).
18. X. Xie et al., "Ion beam machining error control and correction for small scale optics," *Appl. Opt.* **50**, 5221 (2011).
19. W. Liao et al., "Microscopic morphology evolution during ion beam smoothing of Zerodur surfaces," *Opt. Express* **22**, 377–86 (2014).
20. Y. Horiike, T. Yamazaki, and M. Shibagaki, "Aluminum reactive ion etching employing CCl4 {+} Cl2 mixture," *Jpn. J.* **21**, 1412–1420 (1982).
21. V. M. Donnelly and A. Kornblit, "Plasma etching: Yesterday, today, and tomorrow," *J. Vac. Sci. Technol. A Vacuum Surf. Film.* **31**(5), 050825 (2013).
22. M. Bernheim and G. Slodzian, "Effect of oxygen on the sputtering of aluminium targets bombarded with argon ions," *Int. J. Mass Spectrom. Ion Phys.* **12**, 93–99 (1973).
23. J. Bauer, F. Frost, and T. Arnold, "Reactive ion beam figuring of optical aluminium surfaces," *J. Phys. D. Appl. Phys.* **50**, 085101 (2017).
24. J. Bauer et al., "Ultra-precision surface figuring of optical aluminium devices," *Adv. Photonics*, I. Aggarwal et al., Eds., Optical Society of America, Zürich, Switzerland (2018).
25. F. Z. Fang et al., "Manufacturing and measurement of freeform optics," *CIRP Ann. Manuf. Technol.* **62**(2), 823–846 (2013).
26. M. Zeuner et al., "Optimisation and characterisation of a TCP type RF broad beam ion source," *Surf. Coatings Technol.* **142–144**, 39–48 (2001).
27. J. Bauer et al., "Improved ion beam tools for ultraprecision figure correction of curved aluminum mirror surfaces correction of curved aluminum mirror surfaces," *J. Astron. Telesc. Instrum. Syst.* **4**(4), 046003 (2018).
28. C. M. Egert, "Roughness evolution of optical materials induced by ion-beam milling," *Proc. SPIE* **1752**, 63–72 (1992).
29. G. P. H. Gubbels et al., "Rapidly solidified aluminium for optical applications," *Proc. SPIE* **7018**, 70183A (2008).
30. R. ter Horst et al., "Diamond turning and polishing tests on new RSP aluminum alloys," *Proc. SPIE* **8450**, 84502M (2012).
31. F. Sohbatzadeh et al., "Characterization of diamond-like carbon thin film synthesized by RF atmospheric pressure plasma Ar/CH4 jet," *Superlattices Microstruct.* **89**, 231–241 (2016).
32. M. Janietz and T. Arnold, "Surface figuring of glass substrates by local deposition of silicon oxide with atmospheric pressure plasma jet," *Surf. Coatings Technol.* **205**, S351–S354 (2011).
33. A. Lehmann et al., "Plasma deposited silicon oxide films for controlled permeation of copper as antimicrobial agent," *Clin. Plasma Med.* **3**, 3–9 (2015).
34. F. Fanelli and F. Fracassi, "Atmospheric pressure non-equilibrium plasma jet technology: general features, specificities and applications in surface processing of materials," *Surf. Coatings Technol.* **322**, 174–201 (2017).
35. S. Rodil and S. Muhl, "Bonding in amorphous carbon nitride," *Diam. Relat. Mater.* **13**, 1521–1531 (2004).
36. A. Majumdar et al., "Chemical composition and bond structure of carbon-nitride films deposited by CH4/N2 dielectric barrier discharge," *Surf. Coatings Technol.* **201**, 6437–6444 (2007).
37. A. Majumdar, G. Scholz, and R. Hippler, "Structural characterization of amorphous hydrogenated-carbon nitride (aH-CNx) film deposited by CH4/N2 dielectric barrier discharge plasma: 13C, 1H solid state NMR, FTIR and elemental analysis," *Surf. Coatings Technol.* **203**, 2013–2016 (2009).
38. R. ter Horst et al., "Directly polished lightweight aluminum mirror," *Proc. SPIE* **7018**, 701808 (2008).
39. K. J. Moeggenborg et al., "Low-scatter bare aluminum optics via chemical mechanical polishing," *Proc. SPIE* **7060**, 706002 (2008).
40. L. Wamboldt et al., "An ultra-low surface finish process for 6061-Al mirrors," *Proc. SPIE* **9451**, 94511X (2015).
41. J. R. McNeil, "Ion beam applications for precision infrared optics," *J. Vac. Sci. Technol.* **20**, 324–326 (1982).
42. P. Dierickx, "Optical quality and stability of 1.8-m aluminum mirrors," *Proc. SPIE* **1931**, 78–84 (1993).
43. R. Soufli, "Smoothing of diamond-turned substrates for extreme ultraviolet illuminators," *Opt. Eng.* **43**(12), 3089–3095 (2004).
44. R. Steinkopf et al., "Metal mirrors with excellent figure and roughness," *Proc. SPIE* **7102**, 71020C (2008).
45. Y. Xu et al., "Smooth surface morphology of hydrogenated amorphous silicon film prepared by plasma enhanced chemical vapor deposition," *Plasma Sci. Technol.* **11**, 569–575 (2009).
46. M. Pasquetti, "Electroless nickel coating applied to large aluminum mirrors: main critical aspects and solutions," *Met. Mirrors* 141–143 (1993).
47. S. L. Folkman and M. Stevens, "Characterization of electroless nickel plating on aluminum mirrors," *Proc. SPIE* **4771**, 254–264 (2002).
48. J. Kinast et al., "Athermal metal optics made of nickel plated AlSi40," *Proc. SPIE* **10563**, 105631J (2017).
49. Y. Li, H. Takino, and F. Frost, "Ion beam planarization of diamond turned surfaces with various roughness profiles," *Opt. Express* **25**(7), 7828 (2017).
50. Y. Li, H. Takino, and F. Frost, "Characteristics of diamond turned NiP smoothed with ion beam planarization technique," *J. Eur. Opt. Soc.* **13**(1), 27 (2017).
51. M. Beier et al., "Fabrication of high precision metallic freeform mirrors with magnetorheological finishing (MRF)," *Proc. SPIE* **8884**, 88840S (2013).
52. A. T. H. Beaucamp, Y. Namba, and R. R. Freeman, "Automated finishing of diamond turned dies for hard X-ray and EUV optics replication," *Key Eng. Mater.* **552**, 115–123 (2013).
53. K. Moeggenborg et al., "Super-polished aluminum mirrors through the application of chemical mechanical polishing techniques," *Proc. SPIE* **6288**, 62880L (2006).

Jens Bauer received his diploma degree in physics and finished his PhD at the Institute of Inorganic Chemistry at the University of Leipzig in 2009. Afterward, he worked in institutional research as well as in several companies with focus on nanomaterial and thin film technology. Since 2014, he has been investigating optical device finishing by ion beam technologies at the Leibniz Institute of Surface Engineering (IOM) in Leipzig. As an author, he has contributed to 27 peer-reviewed papers.

Frank Frost received his doctorate from the University of Leipzig in 1998. His research focuses on fundamental investigations of the manufacturing of nano- and microstructures using (reactive) ion beam etching (RIBE), pattern formation due to ion beam driven self-organization, the use of ion beam processes for smoothing and planarization down to sub 0.1 nm surface roughness level, and the implementation of these technologies in production practice. He has authored/coauthored more than 130 papers.

Antje Lehmann received her doctorate at the Institute of Materials Science and Technology from the TU Bergakademie Freiberg in 2015. Her research focused on plasma analysis of atmospheric plasma jets, thin film deposition and analysis at the Leibniz Institute of Surface Engineering (IOM) in Leipzig. She has contributed to 12 peer-reviewed articles as an author/coauthor. Since 2019, she has been working in the field of materials science and materials testing at the Pforzheim University.

Melanie Ulitschka received her engineering sciences bachelor's degree in industrial engineering specializing in material engineering and plastics technology. She received her master's degree in composite materials from Hof University of Applied Sciences. She worked from 2015 to 2017 as a research assistant at the Institute

for Materials Science in Hof. Since 2017, she has been a research assistant and doctoral candidate at Leibniz Institute of Surface Engineering in Leipzig.

Yaguo Li received his doctorate Akita Prefectural University, Japan, in 2014. He worked as a Leibniz-DAAD research fellow at Leibniz Institute of Surface Engineering (IOM), Germany in 2016/2017. He is now a group leader at Fine Optical Engineering Research Center, China. His research interests include optical fabrication and laser-induced damage in optics, as well as laser manufacturing and ion machining.

Thomas Arnold has been active in the area of ultraprecision surface machining for more than 20 years. His current research interests include technology development for optical freeform surface fabrication by ion beams as well as chemically reactive plasma jets targeting form accuracy in the nanometer range. He is the author of 30 peer-reviewed papers. Since 2014 he has been endowed professor for ultraprecision surface machining using ions and plasmas at Technische Universität Dresden, Germany.